

Temporally multiplexed ion-photon quantum interface via fast ion-chain transport

Bingran You,^{1,2} Qiming Wu,^{1,2,*} David Miron,^{1,2} Wenjun Ke,¹
Inder Monga,² Erhan Saglamyurek,^{1,2} and Hartmut Haeffner^{1,2,†}

¹*Department of Physics, University of California, Berkeley, CA 94720, USA*

²*Lawrence Berkeley National Laboratory, Berkeley, CA 94720, USA*

(Dated: May 20, 2024)

High-rate remote entanglement between photon and matter-based qubits is essential for distributed quantum information processing. A key technique to increase the modest entangling rates of existing long-distance quantum networking approaches is multiplexing. Here, we demonstrate a temporally multiplexed ion-photon interface via rapid transport of a chain of nine calcium ions across 74 μm within 86 μs . The non-classical nature of the multiplexed photons is verified by measuring the second-order correlation function with an average value of $g^{(2)}(0) = 0.060(13)$, indicating negligible crosstalk between the multiplexed modes. In addition, we characterize the motional degree-of-freedom of the ion crystal after transport and find that it is coherently excited to as much as $\bar{n}_\alpha \approx 110$ for the center-of-mass mode. Our proof-of-principle implementation paves the way for large-scale quantum networking with trapped ions, but highlights some challenges that must be overcome.

Remote entanglement across distant quantum nodes [1, 2] may be used for long-distance quantum key distribution [3, 4], modular quantum computer architectures [5, 6], as well as quantum enhanced metrology and sensing [7–9]. Light-matter quantum interfaces are a fundamental building block for such applications, and allow for distributed entanglement between stationary matter qubits by using "flying" photons.

For practical purposes, these quantum interfaces need to be capable of establishing remote entanglement at high rates across a large-scale network of quantum nodes. However, in widely adopted probabilistic schemes based on heralded photon detection [10–12], it is infeasible to distribute entanglement at useful rates over a few kilometers, as the attempt rate is limited by the round-trip travel-time of photons in a single mode. For example, for a communication distance of 10 km, photon-travel time will be around 100 μs , meaning that the attempt cannot be higher than 10 kHz. In this scenario, even with use of a state-of-the-art photon-matter interface that can yield close to unity photon extraction efficiency [13], the matter-photon entanglement rate beyond tens of kilometers would be limited to sub 10 s^{-1} with total loss around 15 dB after considering the collective probability of generating and detecting telecom photons at each node, along with the optical fiber loss [14, 15].

A key solution to this challenge is multiplexing: to combine multiple signals into a single channel and therefore increase the attempt rate [16, 17]. Multiplexing has become a mature technology for ensemble-based quantum interfaces, both in atomic gases and rare-earth ion doped solid-state systems [18–21]. However, large-scale local quantum information processing is technically challenging in these platforms [22].

In contrast, single emitters, including trapped ions and neutral atoms, offer excellent local quantum information processing capability beside their natural interface with

light at convenient wavelengths for quantum frequency conversion (QFC) [23, 24], and the possibility of long-lived storage of entanglement [25, 26]. On the other hand, implementing a multiplexed light-matter interface with these systems is technically challenging. Towards overcoming this problem, a few multiplexing schemes have already been proposed for ion and atom-based quantum processors [27–30]. The only reported experimental work, we are aware of, is the demonstration of multiplexing using a static three-ion chain [15]. In view of the recent advances of the quantum CCD architecture [31–33], a complementary approach to multiplexing is the process of ion-transport through a specific spatial location with maximized photon coupling efficiency.

In this work, we demonstrate a temporal multiplexing scheme based on the transport of an ion-chain for improving the rate of ion-photon entanglement over long distances. In our experiments, we generate on-demand single photons by shuttling a nine-ion chain across the focus of a single-ion addressing beam. This scheme is expected to lead to a nearly nine-fold increase in attempt rate of the entanglement generation for quantum repeater nodes separated by >100 km. We verify the single-photon nature of the photon trains by measuring a second-order time correlation of $g^{(2)}(0) = 0.060(13)$ without background subtraction. Furthermore, we address the problem of motional excitation during the transport, which is detrimental to local entangling operations [34] and in the case of using a cavity for stimulating the photons would lead to uncertainty in the coupling strength. [35]. Using a shuttling function designed to mitigate motional excitation, we find coherent excitation of $\bar{n}_\alpha \sim 50$ on the center-of-mass (COM) mode during one round of ion chain transport. These results show that the proposed multiplexing scheme can be scaled up to higher rates provided that more optimal transport methods are applied.

The schematics of the experimental procedures is illus-

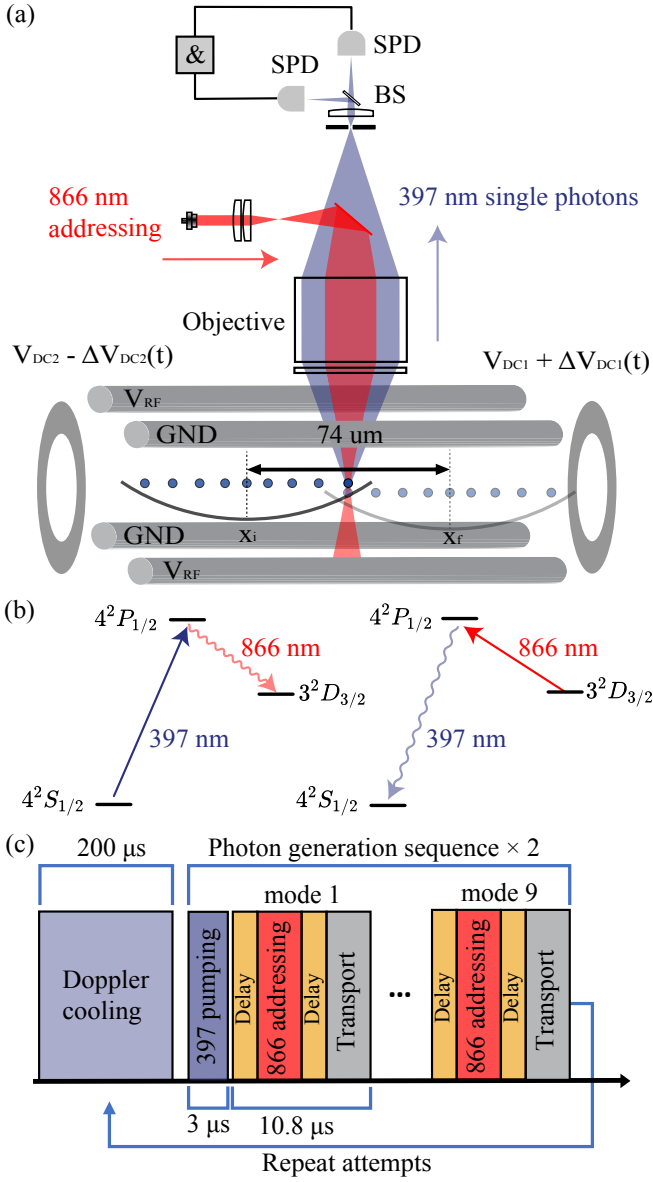


FIG. 1. Schematics of multiplexed ion-photon interface. (a) A nine-ion chain is confined in an RF Paul trap. Controlling DC endcap voltages allows for ion transport. A beam of 397 nm and 866 nm light illuminating all ions is used for Doppler cooling. An objective collects the 397 nm single photons and guides them to a 50/50 beamsplitter, followed by a photomultiplier tube on each exit port for photon detection. An 866 nm beam is focused down to $\approx 6.0 \mu\text{s}$ waist to address individual ions. (b), (c) Excitation scheme and pulse sequence for the 397 nm single-photon generation. First, a global 397 nm beam prepares the ions to the $3^2D_{3/2}$ state. Then, the 866 nm addressing beam (resonance with $3^2D_{3/2} \leftrightarrow 4^2P_{1/2}$) is stroboscopically switched on during the transport to extract photons from the target ions.

trated in Fig. 1(a). Our experiment is conducted using an RF Paul trap, composed of four RF blades for generating radial pseudopotential and two DC endcap electrodes for

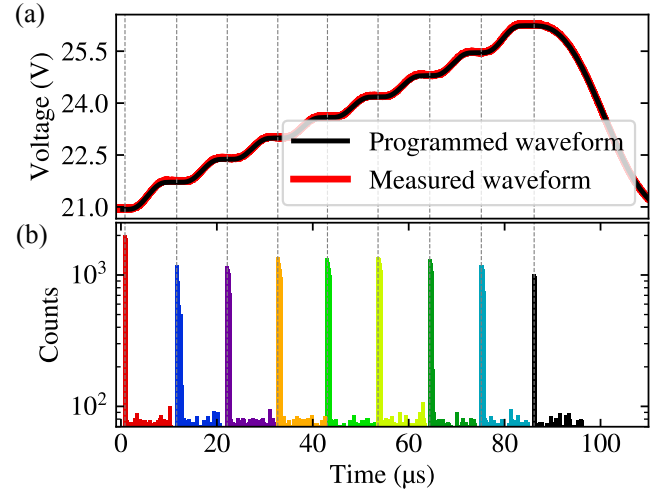


FIG. 2. Temporal profile of single-photon generation. (a) The black (red) line is the programmed (measured) voltage ramp on endcap 1 during the forward transport, showing negligible latency effect. The voltage on endcap 2 is an inverse function of endcap 1 with an offset of $+2.51 \text{ V}$. Not shown is the ramp shuttling the ions back to the original position. (b) Detection time of the photons (bin with 250 ns) color coded with the associated temporal mode.

providing an axial harmonic confinement. We typically trap a string of nine $^{40}\text{Ca}^+$ ions in a linear configuration with the COM mode frequency of $\omega_{x,z}/(2\pi) = \times \{1.15, 0.179\} \text{ MHz}$ and Lamb-Dicke (LD) parameters of the axial modes, ranging between 0.09 and 0.23 on the $4^2S_{1/2} \leftrightarrow 3^2D_{5/2}$ transition. Two global laser beams at 397 nm and 866 nm (not shown in the figure) evenly illuminate the entire ion chain for Doppler cooling and optical pumping, and a tightly focused addressing beam at 866 nm allows for resonant excitation to extract the 397 nm single photons from individual ions. The generated single photons are collected by an objective with a numerical aperture of $\text{NA} = 0.3$ (collection efficiency $P_c \approx 2.5\%$) and directed to a 50/50 beam splitter (BS). At the exit port of BS, photons are detected by two photomultiplier tube (PMT)-based single-photon detectors (SPD), and their arrival times are recorded with a time-tagger for subsequent analysis.

We generate on-demand single-photons based on a background-free scheme, as illustrated in Fig. 1(b) [36]. In this process, we first Doppler cool (detuning $\Delta = -\Gamma/2$) the ion chain for $200 \mu\text{s}$, with the first $100 \mu\text{s}$ assisted by another beam -500 MHz detuned from the $4^2S_{1/2} \leftrightarrow 4^2P_{1/2}$ transition (not shown) to mitigate collision induced ion chain melting in the Paul trap [37]. Then we begin the photon generation sequences with optical pumping to the $3^2D_{3/2}$ state for $3 \mu\text{s}$, followed by transport of the chain to position each ion in the tight focus of the 866 nm addressing beam resonant with $3^2D_{3/2} \leftrightarrow 4^2P_{1/2}$ transition to generate 397 nm single

photons (see Fig. 1(c)).

In the ion-chain transport process, the endcap voltages are controlled by an arbitrary waveform generator (AWG) amplified by a custom-made, low-noise amplifier circuit with a gain of ten through low-pass filters and a vacuum feedthrough. The low-pass filters have cutoff frequencies of 1.9 MHz to allow fast transport of the ion chain close to the speed of the COM mode frequency. The programmed and the measured waveform show a negligible latency effect from the filters (Fig. 2(a)). The forward shuttling function has eight steps, during each of which a different ion is placed in the focus of the addressing beam

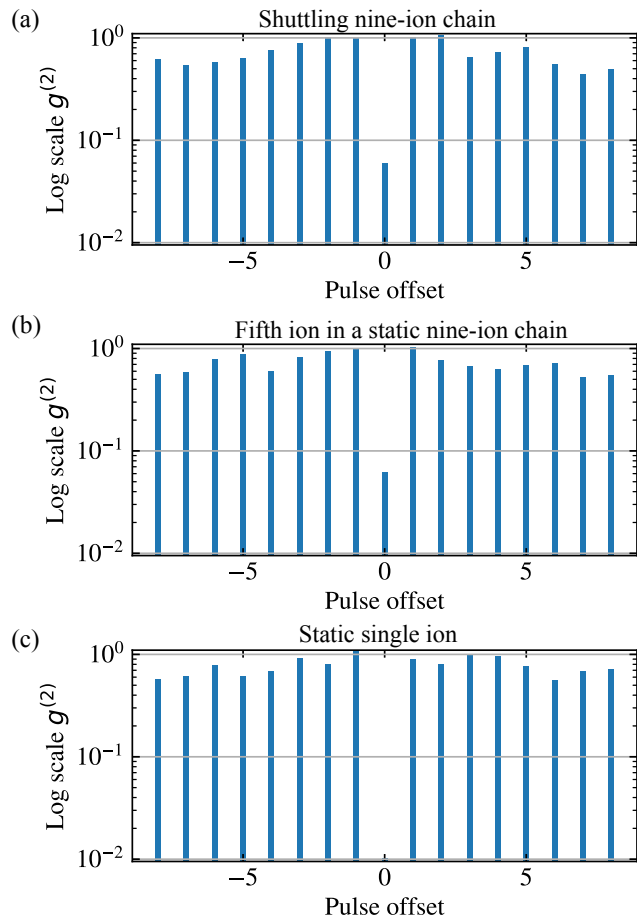


FIG. 3. Two-photon correlation measurements. (a) $g^{(2)}$ measurement when shuttling a nine-ion chain, $g^{(2)}(0) = 0.060(13)$. The horizontal axis represents the delay between individual photons corresponding to the time between each voltage step. The shuttling function in Fig. 2 is repeated twice before the next cooling cycle (see Fig. 1). (b) $g^{(2)}$ measurement when addressing the fifth ion in a static nine-ion chain shows $g^{(2)}(0) = 0.062(17)$. There are 25 attempts after each cooling cycle. The horizontal axis represents the delay time between attempts on the same ion. (c) $g^{(2)}$ measurement of a single ion with the addressing beam using the same pulse sequence as (b). The measured $g^{(2)}(0) = 0.010(6)$. The horizontal axis is the same as (b).

for 1.7 μs with the beam turned on simultaneously. After completing this sequence, we move the entire ion chain back to the original position in 35 μs using the same function form in one step. The voltage ramping function on the two endcaps $V_{1,2}(t)$ is in the form of a sigmoid-like polynomial function such that the first and second order derivative at the beginning and the end of the transport vanish [38].

$$\begin{aligned} V_{\text{DC1}}(t) &= V_{\text{DC1}} + \Delta V \left(10 \left(\frac{t}{T} \right)^3 - 15 \left(\frac{t}{T} \right)^4 + 6 \left(\frac{t}{T} \right)^5 \right) \\ V_{\text{DC2}}(t) &= V_{\text{DC2}} - \Delta V \left(10 \left(\frac{t}{T} \right)^3 - 15 \left(\frac{t}{T} \right)^4 + 6 \left(\frac{t}{T} \right)^5 \right), \end{aligned} \quad (1)$$

where ΔV is the voltage difference between the beginning and the end of a step, t is the time after the end of the previous step, and $T = 9.1 \mu\text{s}$ is the total time of each transport. The details of voltage optimization and numerical simulation of motional heating can be found in [39]. We reconstruct the temporal profile of 397 nm photons during transport using the recorded arrival times of photons on the PMTs. Fig 2(b) shows the emission from individual ions (modes). Data is accumulated for 40 min, during which around 1.56×10^6 attempts were made to the whole string, corresponding to attempt rate 39.0 kHz, an average photon extraction efficiency of 0.21 % and single photons count rate of around 71 cps.

Next, we perform a two-photon correlation experiment to test the non-classical characteristics of our multiplexed photon source [40]. The probability of two-photon correlation when detecting a correlation event on two detectors at different times is given by

$$\rho_c(\tau) = \rho_1(\tau)\rho_2(\tau + \delta T), \quad (2)$$

where $\rho_1(\tau)$ and $\rho_2(\tau + \delta T)$ are the probability of detecting a photon at $t = \tau$ and $\tau + \delta T$ on detector 1 and 2. Fig. 3(a) shows the normalized correlation counts as a function of the delay mode window. We choose a coincidence window of 300 ns in each mode and measure 8 coincident counts at zero delay in 4.8 hours, corresponding to $g^{(2)}(0) = 0.060(13)$. The residual correlation can be explained by excitation of neighboring ions, i.e., crosstalk of the addressing beam, which is separately characterized to be 0.99 % using fluorescence of the nine-ion chain on the camera, corresponding to expected average $g_{\text{exp}}^{(2)}(0) = 0.049(8)$ (see Supplemental [39]). To further verify this hypothesis, we repeat the measurement with a single ion (Fig. 3(c)) and compare it to addressing only the fifth ion in a static nine-ion chain (Fig. 3(b)). The two experiments yield $g^{(2)}(0) = 0.010(6)$ and $g^{(2)}(0) = 0.062(17)$ with 6.0 and 4.8 hours of data accumulation, respectively. While the single ion g_2 is limited by the detector dark counts and ambient light, the measurement of the static 9-ion chain g_2 is limited by the crosstalk of the addressing beam. The results indicate the major source of residual correlation is addressing crosstalk [39]. This

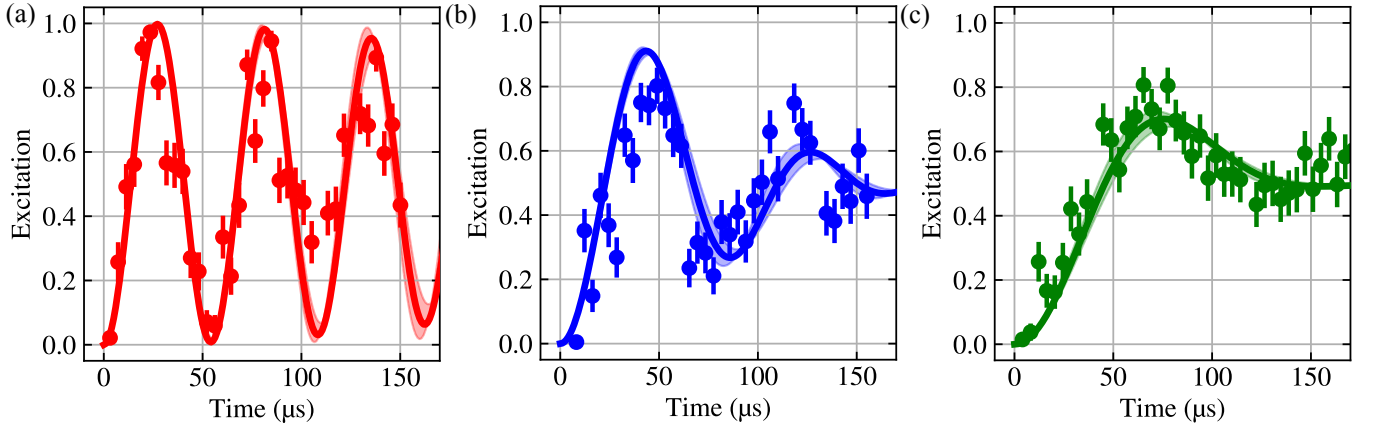


FIG. 4. $|\downarrow\rangle \leftrightarrow |\uparrow\rangle$ carrier excitation of nine-ion chain before and after shuttling. The horizontal axis is the global 729 nm beam probe time, and the vertical axis is the average ion excitation on the $|\uparrow\rangle$ state. Error bars denote one standard deviation of the quantum projection noise. (a) Rabi oscillations of the sideband-cooled ions (red dots). The red line is a numerical simulation of thermal distribution with $\bar{n}_{th} = 4.0 \pm 3.0$. (b) Rabi oscillation after the transport at half speed of the transport function in Fig. 2(a). The blue line is a numerical simulation with $\bar{n}_{th} = 4$, $\bar{n}_\alpha = 50 \pm 5$. (c) Rabi oscillation after the transport at full speed. The green line is a numerical simulation with $\bar{n}_{th} = 4$, $\bar{n}_\alpha = 110 \pm 5$.

can be mitigated by coupling the single photons into a single-mode fiber or improving the optical quality of the excitation beam.

After characterizing the single-photon nature of the transport-multiplexing scheme, we characterize the motion of the ions introduced by shuttling. This is important as the quality of subsequent quantum operations on the ions or ion-photon entanglement will depend on the ions' motional states. We further explore the system performance by measuring the motional heating from the ion transport. To do this, we first perform sideband cooling for all axial modes sequentially using the method similar to that in [41] and prepare the ion in the state $|\downarrow\rangle = |4^2S_{1/2}, m_J = -1/2\rangle$. We compare the $|\downarrow\rangle \leftrightarrow |\uparrow\rangle = |3^2D_{1/2}, m_J = -1/2\rangle$ carrier transition before and after transport with a global 729 nm beam along the axial direction to determine how the transport affects the ion-motion (Fig. 4). The carrier Rabi flopping is motional state sensitive, and the Hamiltonian has the form of [42, 43]

$$H_{i,M} = (\hbar/2)\Omega^{(i)}\sigma_x^{(i)} \prod_{m=1}^M \exp[i\eta_{i,m} [a_m + a_m^\dagger]], \quad (3)$$

where $\Omega^{(i)}$ is the Rabi frequency of the i th ion, a_m and a_m^\dagger are the creation and annihilation operators on the m th mode, and $\eta_{i,m}$ is the LD parameter of the i th ion and the m th mode. Considering the computational difficulty of including all motional modes in the simulation, we only consider the COM mode which we expect to be excited most because the electric fields, both from the transport and surface noise, are correlated over the whole ion string (see Supplemental [39]). Therefore, the average carrier

Rabi flopping can be simplified to

$$P_e(t) = \frac{1}{2N} \left[1 - \sum_{n=0}^{\infty} \sum_{i=0}^N P_n \cos(\Omega_n^{(i)} t) \right], \quad (4)$$

where P_n is the occupation on the n th number state and encodes a convolution between a thermal and a coherent phonon distribution [44]. $\Omega_n^{(i)}$ is the Rabi frequency of the i th ion on the n th number state [45]. To verify the effectiveness of our approximation, we probe the sideband-cooled motional spectrum of the nine-ion chain before the transport and verify that only the COM mode is not cooled to near the ground state [39], for which we find a cooling limit of $\bar{n}_{th} = 4.0 \pm 3.0$. We also measure the electric-field noise induced heating and find a heating rate of 20 quanta/ms. (Fig. 4(a)), indicating that the remaining thermal population is likely limited by the COM mode heating which scales as ion number N [46]. Fig. 4(b) shows the carrier Rabi flopping after ion transport twice as slow as in Fig. 2(a). From numerical simulations (blue line), we find that the data can be explained well by a coherent state $\bar{n}_\alpha = |\alpha|^2 \approx 50$ on the COM mode after the transport. Similarly, we perform the full-speed transport and the carrier Rabi flopping matches with COM coherent state with $\bar{n}_\alpha \approx 110$ (Fig. 4(c)). As shown in the Rabi flopping plots, there is mismatch between the experimental data and numerical simulation at full speed, which could be due to thermal and coherent occupation of other modes and will require additional investigation. For example, one can use an individual 729 nm addressing beam to probe the blue sideband transition of different modes [47]. The optimal fast transport of a long ion chain remains an open question and is beyond the scope of this work. However, we note that further optimization can be done by energy

self-neutral shuttling [31, 44], implementing closed-loop optimization of the shuttling function [48], etc.

To summarize, we have presented a multiplexed ion-photon interface by transporting a nine-ion chain with synchronized excitation in sub-hundred μs . The speed is restricted by the motional frequency and can be increased by an order of magnitude, for instance, using a 3D-printed ion trap [49] with radial frequency beyond 10 MHz. The 397 nm photon can be converted to the telecommunication band via a two-step QFC [24]. Once integrated with state preparation on $3^2D_{3/2}$ Zeeman sub-level and photon collection with a single mode fiber, we expect a faster photon extraction rate [50] and negligible ion crosstalk while achieving high fidelity ion-photon entanglement [51, 52]. Our system can also be combined with a miniature cavity [35] for much higher photon extraction efficiency without sacrificing the photon generation rate, while the ion's positional spread caused by coherent excitation can be mitigated by aligning the cavity along the radial direction or further optimization of the shuttling function. These results stimulate the research of fast shuttling of a chain of tens of ions as a unit cell of logical qubit with heralded entanglement [28] and high-rates entanglement of quantum processors across large distances.

B.Y and Q.W have contributed equally to this work. We thank Alp Sipahigil, Ben Lanyon, Tracy Northup, You-Wei Hsieh, and Wenji Wu for their helpful discussion. Q.W. and H.H. acknowledge funding by the U.S. Department of Energy, Office of Science, Office of Basic Energy Sciences under Awards No. DE-SC0023277. This work is supported by the Office of Science (S.C.) in Advanced Scientific Computing Research (ASCR) through FOA - Quantum Internet to Accelerate Scientific Discovery (LAB 21-2495) and by NSF Grant No. 2016245.

* qiming.wu@berkeley.edu

† hhaeffner@berkeley.edu

- [1] H. J. Kimble, The quantum internet, *Nature* **453**, 1023 (2008).
- [2] L.-M. Duan, M. D. Lukin, J. I. Cirac, and P. Zoller, Long-distance quantum communication with atomic ensembles and linear optics, *Nature* **414**, 413 (2001).
- [3] T. van Leent, M. Bock, F. Fertig, R. Garthoff, S. Eppelt, Y. Zhou, P. Malik, M. Seubert, T. Bauer, W. Rosenfeld, *et al.*, Entangling single atoms over 33 km telecom fibre, *Nature* **607**, 69 (2022).
- [4] D. P. Nadlinger, P. Drmota, B. C. Nichol, G. Araneda, D. Main, R. Srinivas, D. M. Lucas, C. J. Ballance, K. Ivanov, E.-Z. Tan, *et al.*, Experimental quantum key distribution certified by bell's theorem, *Nature* **607**, 682 (2022).
- [5] C. Monroe, R. Raussendorf, A. Ruthven, K. R. Brown, P. Maunz, L.-M. Duan, and J. Kim, Large-scale modular quantum-computer architecture with atomic memory and photonic interconnects, *Physical Review A* **89**, 022317 (2014).
- [6] J. P. Covey, H. Weinfurter, and H. Bernien, Quantum networks with neutral atom processing nodes, *npj Quantum Information* **9**, 90 (2023).
- [7] P. Komar, E. M. Kessler, M. Bishof, L. Jiang, A. S. Sørensen, J. Ye, and M. D. Lukin, A quantum network of clocks, *Nature Physics* **10**, 582 (2014).
- [8] B. Nichol, R. Srinivas, D. Nadlinger, P. Drmota, D. Main, G. Araneda, C. Ballance, and D. Lucas, An elementary quantum network of entangled optical atomic clocks, *Nature* **609**, 689 (2022).
- [9] X. Guo, C. R. Breum, J. Borregaard, S. Izumi, M. V. Larsen, T. Gehring, M. Christandl, J. S. Neergaard-Nielsen, and U. L. Andersen, Distributed quantum sensing in a continuous-variable entangled network, *Nature Physics* **16**, 281 (2020).
- [10] D. L. Moehring, P. Maunz, S. Olmschenk, K. C. Younge, D. N. Matsukevich, L.-M. Duan, and C. Monroe, Entanglement of single-atom quantum bits at a distance, *Nature* **449**, 68 (2007).
- [11] J. Hofmann, M. Krug, N. Ortegel, L. Gérard, M. Weber, W. Rosenfeld, and H. Weinfurter, Heralded entanglement between widely separated atoms, *Science* **337**, 72 (2012).
- [12] H. Bernien, B. Hensen, W. Pfaff, G. Koolstra, M. S. Blok, L. Robledo, T. H. Taminiau, M. Markham, D. J. Twitchen, L. Childress, *et al.*, Heralded entanglement between solid-state qubits separated by three metres, *Nature* **497**, 86 (2013).
- [13] J. Schupp, V. Krcmarsky, V. Krutyanskiy, M. Meraner, T. Northup, and B. Lanyon, Interface between trapped-ion qubits and traveling photons with close-to-optimal efficiency, *PRX quantum* **2**, 020331 (2021).
- [14] V. Krutyanskiy, M. Canteri, M. Meraner, J. Bate, V. Krcmarsky, J. Schupp, N. Sangouard, and B. P. Lanyon, Telecom-wavelength quantum repeater node based on a trapped-ion processor, *Physical Review Letters* **130**, 213601 (2023).
- [15] V. Krutyanskiy, M. Canteri, M. Meraner, V. Krcmarsky, and B. Lanyon, Multimode ion-photon entanglement over 101 kilometers, *PRX Quantum* **5**, 020308 (2024).
- [16] T. Pittman, B. Jacobs, and J. Franson, Single photons on pseudodemand from stored parametric down-conversion, *Physical Review A* **66**, 042303 (2002).
- [17] F. Kaneda, B. G. Christensen, J. J. Wong, H. S. Park, K. T. McCusker, and P. G. Kwiat, Time-multiplexed heralded single-photon source, *Optica* **2**, 1010 (2015).
- [18] Y. Pu, N. Jiang, W. Chang, H. Yang, C. Li, and L. Duan, Experimental realization of a multiplexed quantum memory with 225 individually accessible memory cells, *Nature communications* **8**, 15359 (2017).
- [19] N. Sinclair, E. Saglamyurek, H. Mallahzadeh, J. A. Slater, M. George, R. Ricken, M. P. Hedges, D. Oblak, C. Simon, W. Sohler, *et al.*, Spectral multiplexing for scalable quantum photonics using an atomic frequency comb quantum memory and feed-forward control, *Physical review letters* **113**, 053603 (2014).
- [20] E. Saglamyurek, M. Grimau Puigibert, Q. Zhou, L. Giner, F. Marsili, V. B. Verma, S. Woo Nam, L. Oesterling, D. Nippa, D. Oblak, *et al.*, A multiplexed light-matter interface for fibre-based quantum networks, *Nature communications* **7**, 11202 (2016).
- [21] S. Zhang, J. Shi, Y. Liang, Y. Sun, Y. Wu, L. Duan, and Y. Pu, Fast delivery of heralded atom-photon quan-

- tum correlation over 12km fiber through multiplexing enhancement, arXiv preprint arXiv:2403.13623 (2024).
- [22] C. E. Bradley, J. Randall, M. H. Abobeih, R. Berrevoets, M. Degen, M. A. Bakker, M. Markham, D. Twitchen, and T. H. Taminiau, A ten-qubit solid-state spin register with quantum memory up to one minute, *Physical Review X* **9**, 031045 (2019).
- [23] V. Krutyanskiy, M. Meraner, J. Schupp, and B. Lanyon, Polarisation-preserving photon frequency conversion from a trapped-ion-compatible wavelength to the telecom c-band, *Applied Physics B* **123**, 228 (2017).
- [24] U. Saha, J. D. Sivers, J. Hannegan, Q. Quraishi, and E. Waks, Low-noise quantum frequency conversion of photons from a trapped barium ion to the telecom o-band, *ACS Photonics* **10**, 2861 (2023), <https://doi.org/10.1021/acsp Photonics.3c00581>.
- [25] P. Wang, C.-Y. Luan, M. Qiao, M. Um, J. Zhang, Y. Wang, X. Yuan, M. Gu, J. Zhang, and K. Kim, Single ion qubit with estimated coherence time exceeding one hour, *Nature communications* **12**, 233 (2021).
- [26] P. Drmota, D. Main, D. Nadlinger, B. Nichol, M. Weber, E. Ainley, A. Agrawal, R. Srinivas, G. Araneda, C. Ballance, *et al.*, Robust quantum memory in a trapped-ion quantum network node, *Physical Review Letters* **130**, 090803 (2023).
- [27] W. Huie, S. G. Menon, H. Bernien, and J. P. Covey, Multiplexed telecommunication-band quantum networking with atom arrays in optical cavities, *Physical Review Research* **3**, 043154 (2021).
- [28] Y. Li and J. Thompson, High-rate and high-fidelity modular interconnects between neutral atom quantum processors, arXiv preprint arXiv:2401.04075 (2024).
- [29] P. Dhara, N. M. Linke, E. Waks, S. Guha, and K. P. Seshadreesan, Multiplexed quantum repeaters based on dual-species trapped-ion systems, *Physical Review A* **105**, 022623 (2022).
- [30] J. Ramette, J. Sinclair, Z. Vendeiro, A. Rudelis, M. Cetina, and V. Vuletić, Any-to-any connected cavity-mediated architecture for quantum computing with trapped ions or rydberg arrays, *PRX Quantum* **3**, 010344 (2022).
- [31] R. Bowler, J. Gaebler, Y. Lin, T. R. Tan, D. Hanneke, J. D. Jost, J. Home, D. Leibfried, and D. J. Wineland, Coherent diabatic ion transport and separation in a multizone trap array, *Physical review letters* **109**, 080502 (2012).
- [32] J. M. Pino, J. M. Dreiling, C. Figgatt, J. P. Gaebler, S. A. Moses, M. Allman, C. Baldwin, M. Foss-Feig, D. Hayes, K. Mayer, *et al.*, Demonstration of the trapped-ion quantum ccd computer architecture, *Nature* **592**, 209 (2021).
- [33] S. Moses, C. Baldwin, M. Allman, R. Ancona, L. Ascarunz, C. Barnes, J. Bartolotta, B. Bjork, P. Blanchard, M. Bohn, *et al.*, A race track trapped-ion quantum processor, arXiv preprint arXiv:2305.03828 (2023).
- [34] A. E. Webb, S. C. Webster, S. Collingbourne, D. Breaud, A. M. Lawrence, S. Weidt, F. Mintert, and W. K. Hensinger, Resilient entangling gates for trapped ions, *Physical review letters* **121**, 180501 (2018).
- [35] H. Takahashi, E. Kassa, C. Christoforou, and M. Keller, Strong coupling of a single ion to an optical cavity, *Physical review letters* **124**, 013602 (2020).
- [36] H. Takahashi, A. Wilson, A. Riley-Watson, F. Oručević, N. Seymour-Smith, M. Keller, and W. Lange, An integrated fiber trap for single-ion photonics, *New Journal of Physics* **15**, 053011 (2013).
- [37] M. W. van Mourik, P. Hrmo, L. Gerster, B. Wilhelm, R. Blatt, P. Schindler, and T. Monz, rf-induced heating dynamics of noncrystallized trapped ions, *Physical Review A* **105**, 033101 (2022).
- [38] A. Tobalina, E. Torrontegui, I. Lizuain, M. Palmero, and J. G. Muga, Invariant-based inverse engineering of time-dependent, coupled harmonic oscillators, *Physical Review A* **102**, 063112 (2020).
- [39] See supplemental materials.
- [40] F. Diedrich and H. Walther, Nonclassical radiation of a single stored ion, *Physical review letters* **58**, 203 (1987).
- [41] Y. Yu, N. R. Hutzler, J. T. Zhang, L. R. Liu, J. D. Hood, T. Rosenband, and K.-K. Ni, Motional-ground-state cooling outside the lamb-dicke regime, *Physical Review A* **97**, 063423 (2018).
- [42] D. J. Wineland, C. Monroe, W. M. Itano, D. Leibfried, B. E. King, and D. M. Meekhof, Experimental issues in coherent quantum-state manipulation of trapped atomic ions, *Journal of research of the National Institute of Standards and Technology* **103**, 259 (1998).
- [43] Q. Wu, Y. Shi, and J. Zhang, Continuous raman sideband cooling beyond the lamb-dicke regime in a trapped ion chain, *Physical Review Research* **5**, 023022 (2023).
- [44] A. Walther, F. Ziesel, T. Ruster, S. T. Dawkins, K. Ott, M. Hettrich, K. Singer, F. Schmidt-Kaler, and U. Poschinger, Controlling fast transport of cold trapped ions, *Physical review letters* **109**, 080501 (2012).
- [45] D. Leibfried, R. Blatt, C. Monroe, and D. Wineland, Quantum dynamics of single trapped ions, *Reviews of Modern Physics* **75**, 281 (2003).
- [46] M. Joshi, A. Fabre, C. Maier, T. Brydges, D. Kiesenhofer, H. Hainzer, R. Blatt, and C. Roos, Polarization-gradient cooling of 1d and 2d ion coulomb crystals, *New Journal of Physics* **22**, 103013 (2020).
- [47] G.-X. Wang, Y.-K. Wu, R. Yao, W.-Q. Lian, Z.-J. Cheng, Y.-L. Xu, C. Zhang, Y. Jiang, Y.-Z. Xu, B.-X. Qi, *et al.*, Simulating the spin-boson model with a controllable reservoir in an ion trap, arXiv preprint arXiv:2402.07461 (2024).
- [48] J. D. Sterk, H. Coakley, J. Goldberg, V. Hietala, J. Lechtenberg, H. McGuinness, D. McMurtrey, L. P. Parazzoli, J. Van Der Wall, and D. Stick, Closed-loop optimization of fast trapped-ion shuttling with sub-quanta excitation, *npj Quantum Information* **8**, 68 (2022).
- [49] S. Xu, X. Xia, Q. Yu, S. Khan, E. Megidish, B. You, B. Hemmerling, A. Jayich, J. Biener, and H. Häffner, 3d-printed micro ion trap technology for scalable quantum information processing, arXiv preprint arXiv:2310.00595 (2023).
- [50] C. Crocker, M. Lichtman, K. Sosnova, A. Carter, S. Scarano, and C. Monroe, High purity single photons entangled with an atomic qubit, *Optics express* **27**, 28143 (2019).
- [51] L. Stephenson, D. Nadlinger, B. Nichol, S. An, P. Drmota, T. Ballance, K. Thirumalai, J. Goodwin, D. Lucas, and C. Ballance, High-rate, high-fidelity entanglement of qubits across an elementary quantum network, *Physical review letters* **124**, 110501 (2020).
- [52] J. O'Reilly, G. Toh, I. Goetting, S. Saha, M. Shalaev, A. Carter, A. Risinger, A. Kalakuntla, T. Li, A. Verma, *et al.*, Fast photon-mediated entanglement of continuously-cooled trapped ions for quantum networking, arXiv preprint arXiv:2404.16167 (2024).

Supplemental material: Temporally multiplexed ion-photon quantum interface via fast ion-chain transport

Bingran You,^{1,2} Qiming Wu,^{1,2,*} David Miron,^{1,2} Wenjun Ke,¹ Inder Monga,² Erhan Saglamyurek,^{1,2} and Hartmut Häffner^{1,2,†}

¹Department of Physics, University of California, Berkeley, CA 94720, USA

²Lawrence Berkeley National Laboratory, Berkeley, CA 94720, USA

(Dated: May 20, 2024)

CONTENTS

I. Crosstalk of addressing laser	1
A. Intensity crosstalk	1
B. Analysis of correlation counts at zero delay	1
II. Ion chain transport	2
A. Voltage levels setting for ions position control	2
B. Numerical simulation of shuttling process	2
III. Sideband cooling for the nine-ion chain	3
A. Cooling scheme	3
B. Spectrum scan	4
C. Carrier Rabi flop after sideband cooling	4
References	5

I. CROSSTALK OF ADDRESSING LASER

In this section, we discuss the characterization of 866 nm addressing light's intensity crosstalk and corresponding correlation counts at zero delay time of our multiplexed photon source. We conclude the residual correlation can be explained by the crosstalk of the addressing beam.

A. Intensity crosstalk

Single ion addressing technique with 729 nm light has been demonstrated for quantum information processing [S1]. In this experiment, we use the objective that is optimized for 729 nm (S6ASS2241, Sill Optics) to focus the 866 nm light to generate single photons from individual ions. To quantify the intensity crosstalk of the nine-ion chain, we position each ion at the center of the addressing beam, systematically vary the beam's power, and record the fluorescence of individual ions using an Electron Multiplying CCD (EMCCD) camera. The correlation between photon scattering rate R_s and laser power P for a two-level system is

$$R_s = \gamma \cdot \frac{s}{2(1+s)}, \quad (\text{S1})$$

where $s = k \cdot P = \frac{P}{P_s \cdot (1 + (2\delta/\gamma)^2)}$ is the saturation parameter, P_s the saturation power, δ the laser detuning from atomic resonance, and γ the decay rate of the excited state [S2]. With 397 nm laser power and detuning fixed, we use this function to co-fit the fluorescence data of center ions and neighbor ions as functions of 866 nm addressing laser power. Therefore, the intensity crosstalk equals k_n/k_1 , with k_1 being the fitted parameter for the center ions and k_n being the fitted parameter for a n th nearest-neighbor ion.

We characterize the crosstalk when the beam is centered on each ion. Fig. S1 illustrate the ratio of laser intensity on the non-addressed (neighbor) ions to the addressed (center) ion of the nine-ion chain. The average intensity crosstalk between the center and the nearest-neighbor ions is calculated to be 0.99%.

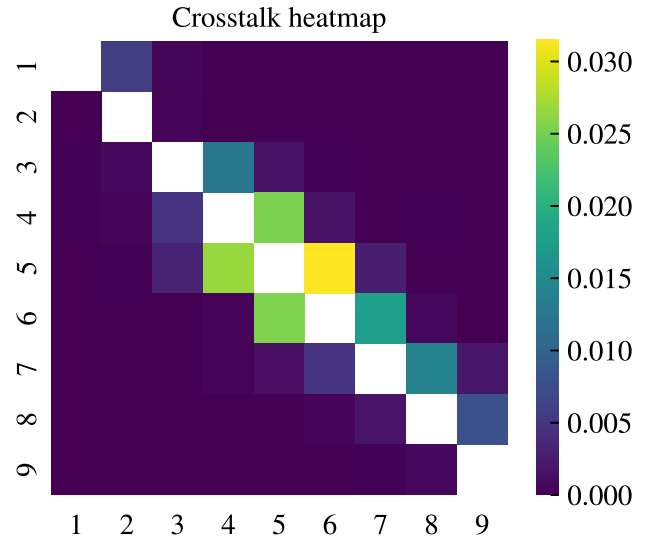


FIG. S1: Heatmap of crosstalk measurement of a nine-ion chain. The average nearest-neighbor intensity crosstalk is around 0.99%.

B. Analysis of correlation counts at zero delay

With the 866 nm addressing beam crosstalk characterization, we estimate the expected residual correlation counts at zero delay time, corresponding to $g^{(2)}(0)$ in the second-order correlation function. We assume for each trial with 866 nm addressing light, the probability of getting one photon from

* qiming.wu@berkeley.edu

† hhaeffner@berkeley.edu

the center ion is ρ_0 , the probability of getting one photon from the two nearest neighbor ions is ρ_{s1} and ρ_{s2} , and the combined contribution of limited collection efficiency and loss along the optical path is ρ_{loss} . For convenience, we use $\tilde{\rho} = \rho \cdot (1 - \rho_{\text{loss}})$. Then, for non-zero delay time, if all other noise sources are ignored, we have correlation probability

$$\rho_c(n) = \left(\frac{\tilde{\rho}_0 + \tilde{\rho}_{s1} + \tilde{\rho}_{s2}}{2} \right)^2, \quad n \neq 0$$

in which there is a factor of 2 in the denominator coming from the BS. For zero delay time, we have

$$\rho_c(0) = \left[2 \left(\frac{\tilde{\rho}_0}{2} \right) \cdot \left(\frac{\tilde{\rho}_{s1} + \tilde{\rho}_{s2}}{2} \right) + 2 \left(\frac{\tilde{\rho}_{s1}}{2} \right) \cdot \left(\frac{\tilde{\rho}_{s2}}{2} \right) \right].$$

Therefore in the limit of small crosstalk, we have

$$g_{\text{exp}}^{(2)}(0) \approx 2 \cdot \frac{\tilde{\rho}_{s1} + \tilde{\rho}_{s2}}{\tilde{\rho}_0} + g_0^{(2)}(0),$$

in which $g_0^{(2)}(0) = 0.010(6)$ corresponds to the contribution of other noise sources other than crosstalk, e.g., detector dark counts and ambient light, that have been characterized by single ion correlation measurement (Fig. 3(c)). Therefore, we expect $g_{\text{exp}}^{(2)}(0) = 0.050(13)$, which is the average $g^{(2)}(0)$ value for nine ions as nine single photon sources. It agrees well with our measurement result of $g^{(2)}(0) = 0.060(13)$ in the multiplexed single-photon generation (Fig. 3(a)).

II. ION CHAIN TRANSPORT

In this section, we illustrate the voltage levels for ion position control and numerical simulation of the shuttling process. Based on the simulation, the center of mass mode has the dominant motional excitation during the ion transport.

A. Voltage levels setting for ions position control

Control of ion positions during fast shuttling is crucial since misaligned ion positions may lead to insufficient photon extraction and increased crosstalk. To precisely align each ion directly at the center of the addressing beam for every voltage step, it is important to understand the ion-ion spacings in the chain. Then, we need to make sure the change in voltage levels matches the corresponding spacing between the ions. In this experiment the two DC endcaps provide the axial confinement. With average voltages of around 24.24 V on the endcaps, the axial trap frequency is around 179 kHz. Combining the Coulomb force and the harmonic potential, the relative equilibrium positions of ions are shown in Fig. S2.

To facilitate the transport of ion chains from one end to the other, we modulate the voltages by increasing voltage on one endcap and decreasing voltage on another while the average voltage remains unchanged. Fig. S3 shows the axial displacement of the trap potential's center as a function of voltage change on both endcaps, indicating a near linear relationship

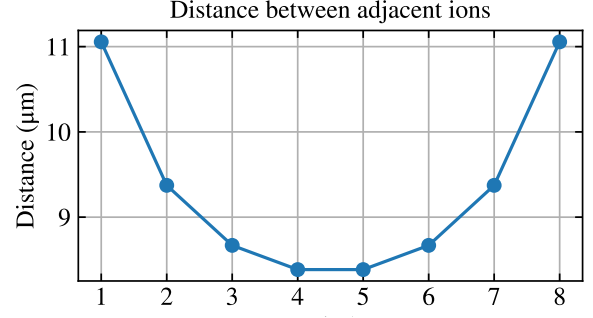


FIG. S2: Nearest-neighbor ion spacing of a nine-ion chain under axial trap frequency of 179 kHz, with average endcap voltage 24.24 V.

between the trap center position and $\Delta V(t)$. Therefore, we program the voltage level changes for each step by referring to the ion-ion spacing, as shown in Fig. S2. Each voltage ramp is following the function form with zero first and second-order derivatives at the beginning and end, as Eqn. 1 in the main text [S3].

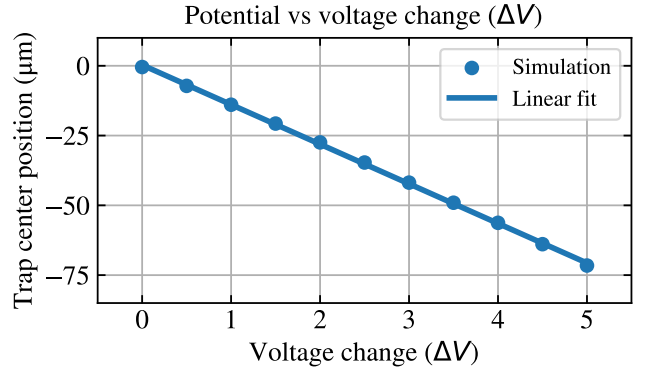


FIG. S3: Relation between axial trap center and endcap voltage change $\Delta V(t)$ with average endcap voltage 24.24 V.

B. Numerical simulation of shuttling process

The nine-ion chain transport can be described by ordinary differential equations (ODE) as

$$\frac{d^2 x_i}{dt^2} = -\omega_0^2 x_i + \frac{kq^2}{m} \sum_{\substack{j=1 \\ j \neq i}}^N \frac{1}{(x_i - x_j)^2} \cdot \text{sgn}(x_i - x_j) \quad (\text{S2})$$

for $i = 1, 2, 3, \dots, N$. In the expression x_i is the position of each ion, ω_0 the trap frequency along axial direction, k the Coulomb's constant, q the charge of electron, and m is the mass of $^{40}\text{Ca}^+$. To simulate this, we calculate the trajectory of each ion by considering a time-dependent trap potential and Coulomb interaction with all other ions. For initial states, the equilibrium positions of each ion are solved using the Newton

method. The equilibrium positions of the nine-ion chain at the beginning are shown in Fig. S2. Then, by simulating the trap potential with finite element method, the temporal function of trap frequency and trap center can be obtained. With the programmed half-speed shuttling function, the positions of all the ions during the transport are shown in Fig. S4. The expected relative amplitudes of 9 motional modes along axial direction at the end of the half-speed shuttling process are shown in Fig. S5, showing only the COM mode is excited in our simulation.

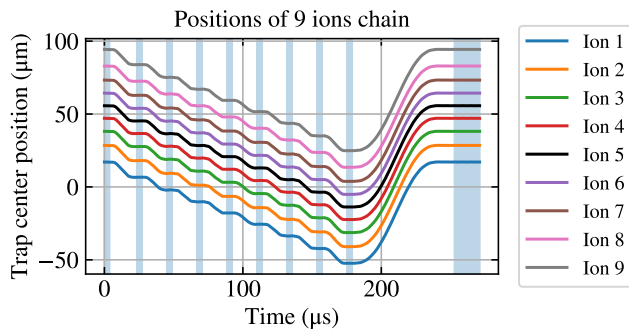


FIG. S4: The positions of 9 ions chain as functions of time. The first 9 narrow blue areas are the time windows where voltage levels stay static. The last blue window is used to measure the motional excitation of all 9 modes at the end of shuttling.

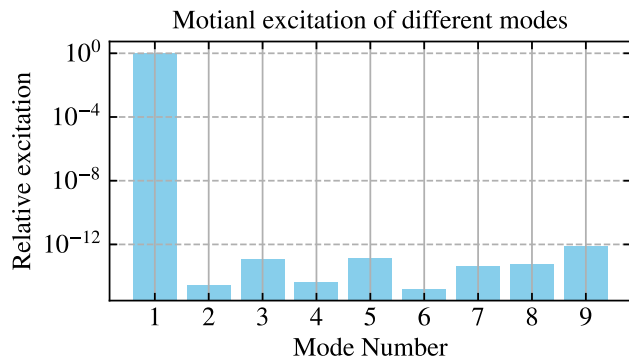


FIG. S5: Relative motional excitation of 9 motional modes along axial direction at the end of the half-speed shuttling process, showing COM mode has the dominant motional excitation.

To better understand the coherent excitation during the ion transport, we numerically simulate the phonon number excitation on the COM mode as a function of the total transport time (Fig. S6). Blue, red and green lines are corresponding to different trap frequency with $\omega_{\text{COM}}/(2\pi) \approx 180$ kHz, 189 kHz, and 198 kHz. The black dash lines mark measurement results for full-speed and half-speed shuttling, while black stars correspond to our measurement results. We can see that the excitation phonon number is very sensitive to

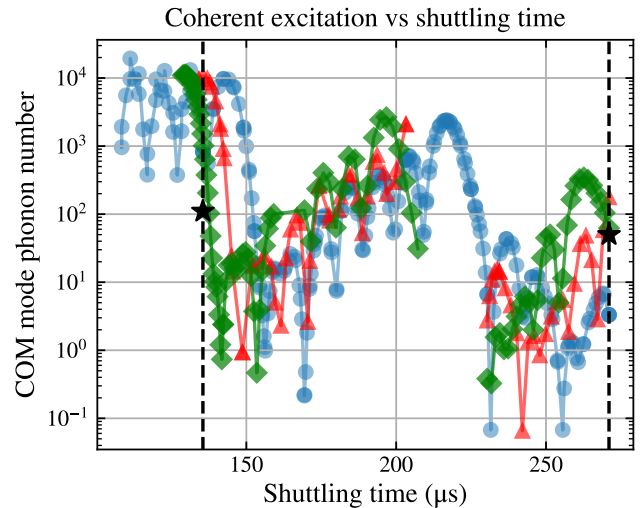


FIG. S6: Numerical simulation for COM mode coherent excitation at the end of shuttling process. Blue, red and green lines are corresponding to different trap frequency with $\omega_{\text{COM}}/(2\pi) \approx 180$ kHz, 189 kHz, and 198 kHz. The black dash lines mark measurement results for full-speed and half-speed shuttling.

variation of the trap frequency and the total transport time, indicating that one reason for the high coherent excitation in our measurement could be the inhomogeneity of the trap potential during the transport. In the future, using a micro-fabricated trap with multiple segmented DC electrodes can help to mitigate this issue.

III. SIDEBAND COOLING FOR THE NINE-ION CHAIN

In this section, we discuss the cooling scheme in this experiment and how thermal heating and coherent excitation influence carrier Rabi flopping with 9 ions.

A. Cooling scheme

We use $|4^2S_{1/2}, m_J = +1/2\rangle \leftrightarrow |3^2D_{1/2}, m_J = -3/2\rangle$ for optical pumping, $|4^2S_{1/2}, m_J = -1/2\rangle \leftrightarrow |3^2D_{1/2}, m_J = -1/2\rangle$ to probe the carrier transition, and $|4^2S_{1/2}, m_J = -1/2\rangle \leftrightarrow |3^2D_{1/2}, m_J = -5/2\rangle$ for sideband cooling. Since the axial COM frequency is as low as 179 kHz, the Doppler cooling limit is around 43 quanta, placing the ions beyond the Lamb-Dicke regime before starting the sideband cooling. So we need to consider the change of red sideband coupling strength at different

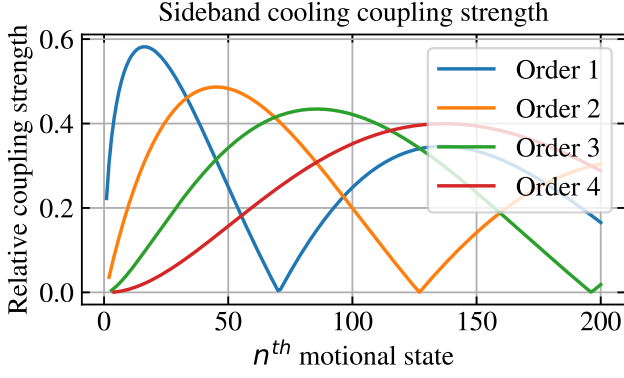


FIG. S7: Relative coupling strength on the carrier and first three orders red sideband for $\eta=0.23$.

motional states

$$\begin{aligned}\Omega_{n-s,n} &= \Omega_0 \left| \langle n-s | e^{i\eta(a+a^\dagger)} | n \rangle \right| \\ &= \Omega_0 e^{-\eta^2/2} \eta^s \sqrt{\frac{(n-s)!}{n!}} L_{(n-s)}^s(\eta^2),\end{aligned}\quad (\text{S3})$$

in which $s (> 0)$ is the order of red sideband [S4]. As shown in Fig. S7, after Doppler cooling, the first-order sideband cooling may have inefficient coupling in a certain range of motional states. Therefore, we first conduct sideband cooling on the second-order red sideband of the three lowest frequency modes and then the first-order red sideband for all the modes. We also use additional cycles for sideband cooling on the COM mode since we found this is the dominant mode for thermal motions by scanning the motional spectrum. All these sideband cooling cycles are performed relative to carrier transition $|4^2S_{1/2}, m_J = -1/2\rangle \leftrightarrow |3^2D_{1/2}, m_J = -5/2\rangle$. On resonance, optical pumping cycles are inserted between and performed at the end.

B. Spectrum scan

After the sideband cooling and optical pumping cycles, we run a full spectrum scan covering the frequency range of all the first-order motional modes along the axial direction. As shown in Fig. S8, even though additional cycles are added for COM mode, it dominates the motional excitation of the crystal after sideband cooling, similar to what has been observed in previous research [S5].

C. Carrier Rabi flop after sideband cooling

The carrier Rabi frequency is modulated according to motional state occupation. In theory, all motional modes need to be taken into consideration since they have different Lamb-Dicke parameters. However, in this experiment, both spectrum scan and shuttling simulation show COM mode dominating the motional excitation. Therefore, we only consider

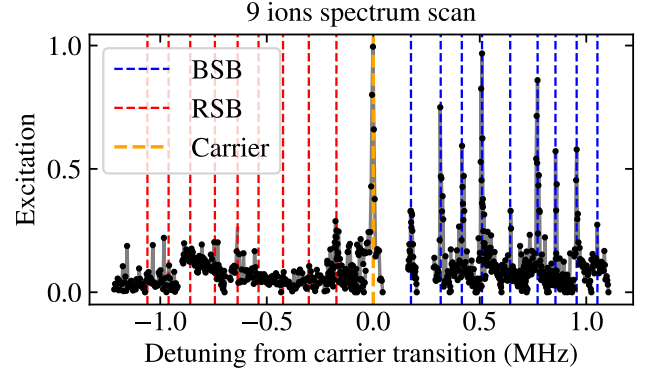


FIG. S8: Motional spectrum after sideband cooling covering carrier, all the 9 RSBs and BSBs.

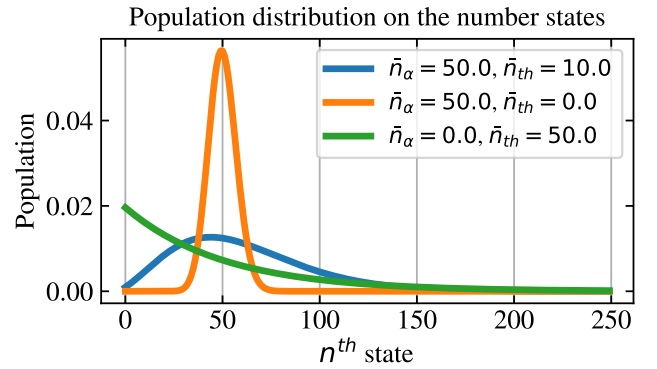


FIG. S9: Population distribution on the number of states under thermal heating, coherent excitation, and both.

the COM mode for fitting carrier Rabi flops to reduce computational complexity. The carrier Rabi frequency is [S6]

$$\Omega_{nn} = \Omega e^{-|\alpha|^2/2} L_n(|\alpha|^2), \quad (\text{S4})$$

in which $\alpha = i\tilde{\eta}e^{i\nu t}$, ν is the trap frequency along the axial direction, $\tilde{\eta}$ is the effective Lamb-Dicke parameter, which for the COM mode $\tilde{\eta} = \eta/\sqrt{N} \approx 0.077$ with N being the number of ions. So the dependence of carrier Rabi frequency on the Lamb-Dicke parameter is

$$\begin{aligned}\Omega_{nn} &= \Omega e^{-\tilde{\eta}^2/2} L_n(\tilde{\eta}^2) \\ &\approx 1 - (n + \frac{1}{2})\tilde{\eta}^2 + (\frac{1}{8} + \frac{n}{4} + \frac{n^2}{4})\tilde{\eta}^4 \\ &\quad - (\frac{1}{48} + \frac{n}{18} + \frac{n^2}{24} + \frac{n^3}{36})\tilde{\eta}^6 + \dots\end{aligned}\quad (\text{S5})$$

Here, we expand the carrier Rabi frequency to the 6th order because of the low trap frequency and high motional heating so that the ions are out of the Lamb-Dicke regime.

While noise sources like surface noise and technical noise will lead to a thermal state, fast shuttling causes coherent excitation. Fig. S9 shows that for coherent excitation, motional states will distribute around the $\tilde{n}_\alpha = |\alpha|^2$ number state, while

thermal heating leads to a Boltzmann distribution of the number states. In the presence of both mechanisms, The phonon

probability follows a convolution of coherent and thermal distribution, which has a much wider distribution over different number states [S7, S8].

-
- [S1] H. C. Nägerl, D. Leibfried, H. Rohde, G. Thalhammer, J. Eschner, F. Schmidt-Kaler, and R. Blatt, Laser addressing of individual ions in a linear ion trap, *Phys. Rev. A* **60**, 145 (1999).
- [S2] P. Van der Straten and H. Metcalf, *Atoms and molecules interacting with light: Atomic physics for the laser era* (Cambridge University Press, 2016).
- [S3] A. Tobalina, E. Torrontegui, I. Lizuain, M. Palmero, and J. G. Muga, Invariant-based inverse engineering of time-dependent, coupled harmonic oscillators, *Physical Review A* **102**, 063112 (2020).
- [S4] D. Leibfried, R. Blatt, C. Monroe, and D. Wineland, Quantum dynamics of single trapped ions, *Reviews of Modern Physics* **75**, 281 (2003).
- [S5] Q. Wu, Y. Shi, and J. Zhang, Continuous raman sideband cooling beyond the lamb-dicke regime in a trapped ion chain, *Physical Review Research* **5**, 023022 (2023).
- [S6] K. E. Cahill and R. J. Glauber, Ordered expansions in boson amplitude operators, *Physical Review* **177**, 1857 (1969).
- [S7] A. Walther, F. Ziesel, T. Ruster, S. T. Dawkins, K. Ott, M. Hettrich, K. Singer, F. Schmidt-Kaler, and U. Poschinger, Controlling fast transport of cold trapped ions, *Physical review letters* **109**, 080501 (2012).
- [S8] F. Ziesel, *Quantum State Manipulation and Dynamics in Micro Ion Traps*, Ph.D. thesis, Universität Ulm (2013).